Measurement-based entanglement of semiconductor spin qubits

Remy L. Delva,[1] Jonas Mielke,[2] Guido Burkard,[2] and Jason R. Petta[3,4]
[1]*Department of Physics, Princeton University, Princeton, New Jersey 08544, USA*
[2]*Department of Physics, University of Konstanz, D-78457 Konstanz, Germany*
[3]*Department of Physics and Astronomy, University of California, Los Angeles, Los Angeles, California 90095, USA*
[4]*Center for Quantum Science and Engineering, University of California, Los Angeles, Los Angeles, California 90095, USA*

(Received 24 December 2023; revised 27 June 2024; accepted 28 June 2024; published 16 July 2024)

Measurement-based entanglement (MBE) is a method for entangling quantum systems through the state projection that accompanies a parity measurement. We derive a stochastic master equation describing measurement-based entanglement of a pair of silicon double-dot flopping-mode spin qubits, develop numerical simulations to model this process, and explore what modifications could enable an experimental implementation of such a protocol. With device parameters corresponding to current qubit and cavity designs, we predict an overlap of the final state of the MBE protocol with the target Bell state $|\Psi_+\rangle$ of ≈61%. By increasing the cavity outcoupling rate by a factor of 10, we are able to obtain an improvement of this metric to ≈81% while maintaining a yield of 33%.

DOI: 10.1103/PhysRevB.110.035304

I. INTRODUCTION

Due to their long spin-coherence times and reliance on proven nanofabrication technologies, electron spin qubits in silicon are strong candidates for use in a quantum computer [1]. Spins generally interact through the exchange interaction, which is based on electrical control of wave function overlap [2]. Previous implementations of two-qubit gates in silicon quantum devices have used tunable exchange couplings to establish interactions between neighboring qubits; these interactions can evolve an unentangled two-qubit state into an entangled state [3–7]. However, for nonadjacent qubit pairs, this type of gate is limited by the short effective range of the exchange interaction.

Spatially separated and entangled qubits are indispensable for various quantum information tasks. The nonlocal correlations inherent in entanglement enable quantum teleportation [8] and quantum key distribution [9,10] over long distances. In distributed quantum computing [11], entangled states connect qubits across physical distances, facilitating scalable architectures and enabling quantum operations on widely separated qubits.

Circuit quantum electrodynamics (cQED) is a device architecture that has enabled strong coupling between microwave frequency photons and superconducting qubits [12,13]. Long-distance coupling of superconducting qubits has also been achieved with cQED [14,15]. Efforts have been made to broaden cQED by incorporating semiconductor quantum dots in microwave cavities [16–18]; strong spin-photon coupling, resonant spin-spin interactions, and dispersive spin-spin coupling have all been experimentally demonstrated [19–24]. Further improvements in device performance may enable the generation of highly entangled spin states with quantum dot cQED.

We can consider two classes of techniques used to generate entanglement in cQED device architectures. The first is to implement a nonlocal entangling gate, such as an iSWAP, by precisely controlling the length of the interaction. Labeling the individual qubits' ground (excited) state by $\downarrow$ ($\uparrow$), an iSWAP gate transforms $|\downarrow\uparrow\rangle \mapsto -i|\uparrow\downarrow\rangle$ and $|\uparrow\downarrow\rangle \mapsto -i|\downarrow\uparrow\rangle$, leaving $|\downarrow\downarrow\rangle$ and $|\uparrow\uparrow\rangle$ unchanged [25,26]. An alternate means of generating entanglement is to exploit the properties of quantum measurement to project an initially unentangled two-qubit state onto an entangled subspace [27]. The second approach is generally referred to as measurement-based entanglement (MBE).

As an example of an MBE protocol, suppose we prepare two qubits in the product state,

$$|\Psi_{\text{init}}\rangle = |+x\rangle|+x\rangle = \tfrac{1}{2}(|\downarrow\downarrow\rangle + |\downarrow\uparrow\rangle + |\uparrow\downarrow\rangle + |\uparrow\uparrow\rangle), \quad (1)$$

where $|+x\rangle = \frac{1}{\sqrt{2}}(|\downarrow\rangle + |\uparrow\rangle)$.

A nondemolition parity measurement of the two-qubit system will produce one of the following maximally entangled Bell states:

$$\text{even parity} \Rightarrow |\Phi_+\rangle = \frac{1}{\sqrt{2}}(|\downarrow\downarrow\rangle + |\uparrow\uparrow\rangle), \quad (2)$$

$$\text{odd parity} \Rightarrow |\Psi_+\rangle = \frac{1}{\sqrt{2}}(|\downarrow\uparrow\rangle + |\uparrow\downarrow\rangle). \quad (3)$$

By repeating this process of initialization and measurement while postselecting on the measured parity, we can obtain a specific two-qubit Bell state. Alternatively, we can condition the application of a single-qubit Pauli x gate upon the measurement of the undesired parity to obtain a specific Bell state deterministically. MBE protocols of the former kind have previously been demonstrated with trapped ions [28], transmon qubits [29], and nitrogen-vacancy centers in diamond [30]. Additionally, experiments with transmon qubits have implemented protocols of the latter kind, in which states of unwanted parity are rotated onto the desired state using unitary gates [31].

Compared to implementations utilizing unitary qubit-qubit interactions, the MBE approach has the potential to be less

demanding in terms of dynamical fine-tuning, since during the measurement process the state will nominally approach one of the states corresponding to a measurement outcome, with a minimum of oscillatory behavior. The lack of direct coupling may also help prevent undesirable qubit-qubit interactions during other stages of a quantum algorithm: effective interactions can be eliminated by simply turning off the measurement signal, without requiring any retuning of qubit parameters. Extensions of the parity-measurement protocol to more than two qubits can also enable the generation of Greenberger-Horne-Zeilinger states with fewer operations, albeit nondeterministically; if conditional unitary corrections are also implemented, MBE can produce such states deterministically [31].

In this paper, we evaluate the feasibility of using dispersive or near-dispersive cQED measurements to implement MBE protocols with semiconductor spin qubits. Previous analyses of superconducting [27,28,30–33] and semiconductor [34] qubit MBE protocols have treated the qubits as ideal two-level systems interacting with a cavity directly through an electric-dipole coupling term. For cavity-coupled semiconductor double quantum dot (DQD) flopping-mode spin qubits, effective spin-photon coupling is instead the result of a combination of electric dipole coupling of a single electron charge to the cavity electric field and synthetic spin-orbit coupling produced by a magnetic field gradient, as shown in Fig. 1(a). As such, a DQD flopping mode spin-qubit device is described by a four-level system consisting of hybridized orbital and spin states [35]. Consequently, a comprehensive theoretical analysis is necessary to explore the feasibility and performance of MBE protocols for semiconductor spin qubit devices. We address this need by simulating the evolution of a system consisting of two cavity-coupled flopping-mode spin qubits that are subjected to a continuous homodyne parity measurement. Each simulation run produces a measurement record and a corresponding postmeasurement system density matrix. We characterize this density matrix by its overlap with the desired target state of the MBE protocol and its concurrence, which indicates the level of entanglement present in the postmeasurement system state.

This paper is structured as follows: Section II characterizes the performance of MBE protocols for two-level qubits that are subjected to parity measurements. In Sec. III, we describe the Hamiltonian governing a system consisting of two cavity-coupled flopping-mode spin qubits. Section IV characterizes the performance of spin-qubit MBE protocols that can be achieved with existing devices. We also estimate the device parameters that will be needed to achieve postselected fidelities $F_{|\Psi_+\rangle} > 80\%$ to the Bell state $|\Psi_+\rangle$. We conclude in Sec. V with a summary of practical alterations to existing cavity designs and an outlook for further work on this subject.

II. MBE FOR TWO-LEVEL SYSTEMS

We first review how an MBE protocol might be implemented for a cQED system using an idealized Hamiltonian. Within this section, we assume that the two-level system constituting the qubit couples directly to the cavity. While this assumption is sufficient to accurately model superconducting cQED, the spin-photon interaction for semiconductor

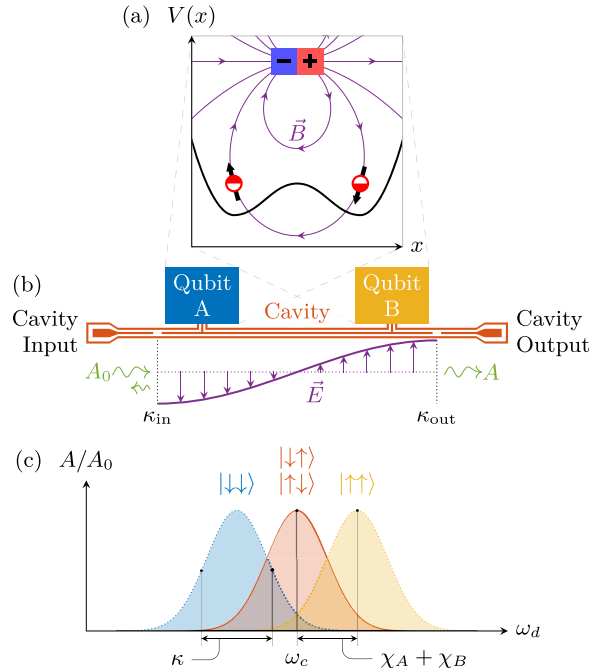

FIG. 1. (a) Illustration of the spin-charge coupling mechanism within a flopping-mode DQD. The presence of a gradient magnetic field $\vec{B}$ causes the Zeeman splitting and quantization axis of the electron spin to depend on its position. This allows the electric field $\vec{E}$ of the microwave cavity to couple to the spin of the electron. (b) Schematic of an MBE device. Qubits A and B are located at the antinodes of a half-wavelength ($\lambda/2$) cavity with input and output couplings κ_{in} and κ_{out}. (c) Illustration of the normalized cavity transmission A/A_0 as a function of cavity drive frequency ω_d for a generic MBE protocol using two-level qubits. The bare cavity-resonance frequency ω_c is shifted by either $\pm(\chi_A + \chi_B)$ for even-parity states or zero for odd-parity states (assuming $\chi_A = \chi_B$). Probing the cavity transmission at ω_c therefore implements a parity measurement.

spin qubits is achieved through a multi-level configuration. This configuration is described in more detail starting in Sec. III.

For two-level qubits A and B coupled to a cavity, as shown in Fig. 1(b), the standard Jaynes-Cummings Hamiltonian is

$$H = \hbar\omega_c \hat{a}^\dagger \hat{a} + \hbar \sum_{j\in\{A,B\}} \left[\frac{\omega_j}{2}\sigma_z^{(j)} + g_j\left(\hat{a}^\dagger \sigma_-^{(j)} + \hat{a}\sigma_+^{(j)}\right)\right], \tag{4}$$

where ω_c is the resonance frequency of the cavity, $\omega_{A(B)}$ are the qubit transition frequencies, and $g_{A(B)}$ are the qubit-cavity coupling rates. Unless specified otherwise, all frequencies are given in units of rad/s. $\sigma_{z,+,-}^{(A(B))}$ are the standard Pauli operators applied to the relevant qubit, and $\hat{a}(\hat{a}^\dagger)$ is the cavity photon annihilation(creation) operator.

In the dispersive regime, i.e., where $g_{A(B)} \ll \Delta_{A(B)}$, the Hamiltonian can be approximated as [36]

$$H_{\text{disp}} = \hbar\left(\omega_c + \sum_{j\in\{A,B\}} \chi_j \sigma_z^{(j)}\right)\hat{a}^\dagger\hat{a} + \sum_{j\in\{A,B\}} \frac{\hbar}{2}(\omega_j + \chi_j)\sigma_z^{(j)} + \hbar J(\sigma_-^{(A)}\sigma_+^{(B)} + \sigma_+^{(A)}\sigma_-^{(B)}), \tag{5}$$

where $J = \frac{g_A g_B(\Delta_A+\Delta_B)}{2\Delta_A\Delta_B}$, $\Delta_j = \omega_j - \omega_c$ are qubit-cavity detunings and $\chi_j = \frac{g_j^2}{\Delta_j}$ are the dispersive shifts for the two qubits [32].

The first term in Eq. (5) implies that the cavity resonance frequency is dispersively shifted by an amount $\sum_{j\in\{A,B\}} \chi_j \sigma_z^{(j)}$ that is dependent on the state of the qubits. Now suppose that the qubit-cavity couplings are set such that $g_A = -g_B = g$, and the qubit-cavity detunings satisfy $\Delta_A = \Delta_B = \Delta$. In this case, the dispersive shifts induced by both qubits are equal. Then, if both qubits are in the ground state such that $|\psi\rangle_{AB} = |\downarrow\rangle_A|\downarrow\rangle_B$, the cavity resonance will be dispersively shifted down in frequency. Similarly, if $|\psi\rangle_{AB} = |\uparrow\rangle_A|\uparrow\rangle_B$, the cavity resonance will be shifted up in frequency. These two cases are shown as the blue and yellow curves in Fig. 1(c), respectively. In contrast, if the qubits are in opposite states the two dispersive shifts will cancel out and the cavity response will be unchanged, as shown by the orange curve in Fig. 1(c). Measurements of the normalized cavity transmission A/A_0 performed with the cavity drive frequency ω_d tuned to the cavity frequency (i.e., with the cavity-drive detuning $\Delta_c = \omega_c - \omega_d = 0$) will depend on the parity of the two qubits.

Two issues must be noted before modeling the parity-measurement process. First, any real qubit will be subject to a noisy environment, causing dephasing and other incoherent evolutions to occur at some rate. The cavity measurement process is not instantaneous, and the assorted qubit and cavity detunings and coupling strengths will similarly establish a rate at which measurement (and the corresponding projection) occurs. A successful experimental implementation must use a set of realistic device and measurement parameters that will allow the qubits to be entangled more quickly than they will decohere; therefore our simulation must model both measurement and decoherence as continuous phenomena.

Second, depending on the regime in which the qubits are operated, the cavity may have other effects on the qubits. The third term in Eq. (5), corresponding to coherent qubit-qubit interactions mediated by virtual cavity photons, is an example of such an effect. Resonant exchange of excitations between a qubit and the cavity also becomes possible if the device leaves the dispersive regime, i.e., if $g \gtrsim \Delta$.

Optimizing the qubit and measurement parameters is therefore crucial for the success of the experiment; the capacity to accurately simulate the influences of various measurement parameters on the final distribution of states is consequently an important step towards an effective experimental realization of MBE.

For a system of two ideal two-level qubits dipole-coupled to a driven cavity, we obtain the following master equation describing the evolution of the combined system in time, with respect to a reference frame obtained by first transforming to the rotating reference frame defined by

$$U = \exp\left[i\left(\sum_{j\in\{A,B\}} \frac{\omega_j \sigma_z^{(j)}}{2} + \omega_d \hat{a}^\dagger \hat{a}\right)t\right], \tag{6}$$

and subsequently transforming to the displaced frame set by $D[\alpha] = \exp(\alpha\hat{a}^\dagger - \alpha^*\hat{a})$:

$$d\rho = \mathcal{L}\rho dt = -\frac{i}{\hbar}[\hat{H}_{\text{eff}}, \rho]dt + \sum_{j\in\{A,B\}} \left(\gamma_1^{(j)}\mathcal{D}[\sigma_-^{(j)}]\rho + \frac{\gamma_\phi^{(j)}}{2}\mathcal{D}\left[\sigma_z^{(j)}\right]\rho\right)dt + \kappa(\mathcal{D}[\hat{a}]\rho)dt. \tag{7}$$

Here $\mathcal{L}$ is a superoperator for the deterministic evolution of ρ and $\mathcal{D}[\mathcal{O}]$ is the dissipation superoperator

$$\mathcal{D}[\mathcal{O}]\rho = \mathcal{O}\rho\mathcal{O}^\dagger - \tfrac{1}{2}\{\mathcal{O}^\dagger\mathcal{O}\}\rho. \tag{8}$$

The effective Hamiltonian is obtained by consecutively transforming H [Eq. (4)] to the frame set by U [Eq. (6)] and $D[\alpha]$,

$$\hat{H}_{\text{eff}} = \hbar\Delta_c\hat{a}^\dagger\hat{a} + \hbar\sum_{j\in\{A,B\}} [g_j e^{i\Delta_j t}(\hat{a} - \alpha)\sigma_+^{(j)} + g_j e^{-i\Delta_j t}(\hat{a}^\dagger - \alpha^*)\sigma_-^{(j)}], \tag{9}$$

with

$$\dot{\alpha} = -i\Delta_c\alpha + i\sqrt{\kappa_{\text{in}}}p(t) - \frac{\kappa}{2}\alpha. \tag{10}$$

Here α is the cavity coherent state population, $\kappa = \kappa_{\text{in}} + \kappa_{\text{out}}$, $p(t)$ is the amplitude of the cavity drive in units of photons per unit time, and $\gamma_1^{(j)}(\gamma_\phi^{(j)})$ is the relaxation(dephasing) rate of qubit j. The terms in Eq. (7) account for the system's coherent evolution, qubit relaxation and dephasing, and cavity loss, respectively. Note that this master equation does not make a dispersive assumption, resulting in the effective Hamiltonian being distinct from Eq. (5).

While Eq. (7) models the system's incoherent behavior, it only provides the unconditioned evolution of the system: the dependence of the final state on the observed measurement outcome is not captured. To associate measurement outcomes with final values of the system's density matrix, we must add a fourth, stochastic term. We can then numerically simulate many specific evolutions of the density matrix, recording the final state of the system and experimental measurement result for each iteration.

A continuous homodyne measurement of the microwave transmission through the cavity described by a measurement efficiency η and phase offset ϕ adds a stochastic term to the master equation [37]. Denoting the conditional density matrix that evolves according to this stochastic differential equation ρ_{cond}, we obtain

$$d\rho_{\text{cond}} = \mathcal{L}\rho_{\text{cond}}dt + \sqrt{\kappa_{\text{out}}\eta}\mathcal{M}[e^{i\phi}\hat{a}]\rho_{\text{cond}}dW(t), \tag{11}$$

with

$$\mathcal{M}[\hat{\mathcal{O}}]\rho = \hat{\mathcal{O}}\rho + \rho\hat{\mathcal{O}}^\dagger - \langle\hat{\mathcal{O}} + \hat{\mathcal{O}}^\dagger\rangle\rho. \tag{12}$$

Here $dW(t)$ is a stochastic variable with zero mean and variance dt. For each sampling (or trajectory) of $dW(t)$, we can then calculate the resulting homodyne output signal V_P,

$$V_P(t)dt \propto \sqrt{\kappa_{\text{out}}\eta}\langle e^{-i\phi}\hat{a}^\dagger + e^{i\phi}\hat{a}\rangle dt + dW(t). \tag{13}$$

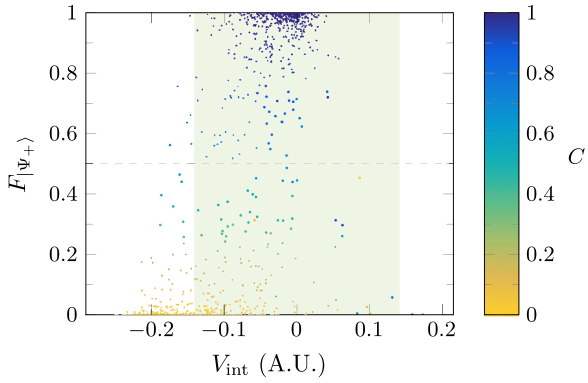

FIG. 2. Scatter plot of the Bell state fidelity $F_{|\Psi_+\rangle}$ as a function of V_{int} using two-level device parameters from Ref. [32], Fig. 4 inset. Defining the measurement rate $\Gamma_{\text{ci}}/2\pi = \frac{g^2\kappa}{\pi\Delta^2} = 0.032\,\text{MHz}$, we have $\omega_d/2\pi = \omega_c/2\pi = 0.796\,\text{MHz}$, $\kappa/2\pi = (\frac{\Delta}{g})^2\frac{\Gamma_{\text{ci}}}{4\pi} = 1.592\,\text{MHz}$, $\Delta/2\pi = 5g/\pi = 15.915\,\text{MHz}$, $p/2\pi = \frac{\Gamma_{\text{ci}}}{16\sqrt{2}\pi} = 2.814\,\text{MHz}$, and $\eta = 1$ (taking $\kappa_{\text{in}}/\kappa_{\text{out}} = 1/8$). This simulation contains 1200 trajectories, shown here at time $t = 5\Gamma_{\text{ci}}^{-1} = 25\,\mu\text{s}$. The point colors correspond to the final-state concurrence C of each trajectory. The shaded green background region indicates the interval where $|V_{\text{int}}| \leqslant t\sqrt{\Gamma_{\text{ci}}}$. This inequality is used to define which measurements are accepted and included in subsequent calculations of the averages of $F_{|\Psi_+\rangle}$ and C shown in Fig. 3. The dashed gray line is a guide to the eye, indicating a fidelity of 50%.

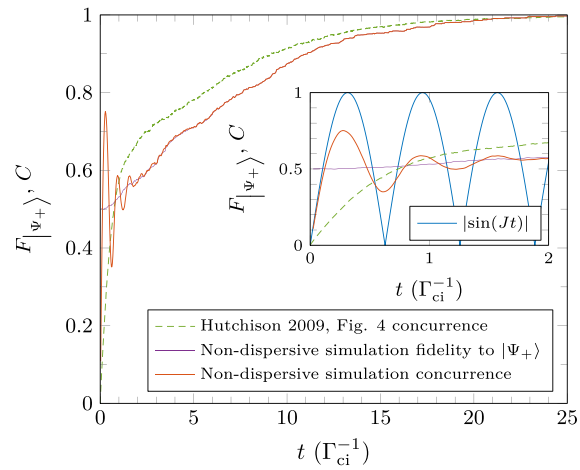

FIG. 3. Fidelity to the target Bell state $F_{|\Psi_+\rangle}$ and concurrence C as a function of time for the ensemble of trajectories corresponding to integrated homodyne signals V_{int} within the shaded green region of Fig. 2, over an evolution time of $t = 25\,\mu\text{s}$. This effectively confines the analysis to trajectories within the high-fidelity cluster near $V_{\text{int}} = 0$. The dashed green line shows results from [32], Fig. 4, specifically in the case where $g^2\kappa/\Delta^2 = \Gamma_{\text{ci}}/2$. The solid orange line shows the results of our non-dispersive simulation of the same two-level system for the same parameters. Note that the oscillatory behavior seen in this plot was not observed in Ref. [32], which used a dispersive approximation in which cavity-mediated qubit-qubit effects were neglected by setting $J = 0$. Inset: An enlarged view of the results for $t \in [0, 2\Gamma_{\text{ci}}^{-1}]$. The light blue line shows the theoretically predicted concurrence according to a dispersive model with fully coherent evolution [see Eq. (24)] and $J = \frac{g_A g_B(\Delta_A+\Delta_B)}{2\Delta_A\Delta_B} = -\frac{g^2}{\Delta}$.

Since the physical homodyne output will depend on experimental specifics such as the amplifier gain, we will use arbitrary units for $V_P(t)$ in the following sections.

The MBE protocol begins with the qubits initialized in the state $|\Psi_{\text{init}}\rangle$ defined in Eq. (1). A constant cavity drive with amplitude $p = \frac{g^2\kappa}{2\sqrt{2}\Delta^2}$ is applied for the duration of the measurement. During each measurement, $V_P(t)$ is integrated over time to produce an associated scalar value V_{int}, which is then used to determine whether the resulting two-qubit state will be retained or discarded. Within the simulation, each of these measurement sequences corresponds to a trajectory of the stochastic master equation, Eq. (11), with an independent random sampling of the stochastic variable $dW(t)$. The full simulation run evaluates 1200 such trajectories using a stochastic Runge-Kutta method similar to that described in Ref. [38]. The concurrence $C[\rho_{\text{red}}]$ [39] and fidelity to the target Bell state $F_{|\Psi_+\rangle} = \text{Tr}[\rho_{\text{red}}|\Psi_+\rangle\langle\Psi_+|]$ are then calculated for the final density matrix of each trajectory, where ρ_{red} is the reduced density matrix obtained by taking the partial trace of ρ_{cond} with respect to the cavity degree of freedom, i.e., $\rho_{\text{red}} = \text{Tr}_{\text{cav}}[\rho_{\text{cond}}]$. These values can then be used to generate scatter plots showing the extent of the correlation between the measurement results (V_{int}) and the final fidelity to the target state ($F_{|\Psi_+\rangle}$).

We first simulate the operation of an idealized two-level device evolving according to Eq. (11). Figure 2 shows a scatter plot of $F_{|\Psi_+\rangle}$ as a function of the integrated homodyne output V_{int} for a given trajectory. Each point corresponds to a single trajectory of Eq. (11). The parameters used in the simulation are listed in the Fig. 2 caption and correspond to those used in previous work describing MBE protocols for superconducting qubits, where $g = g_A = -g_B$ and $\Delta = \Delta_A = \Delta_B$ [32].

We can assess the performance of the entanglement procedure by examining Fig. 2. First, note the two dense clusters of points, one with high C near $V_{\text{int}} = 0$ and the other with low C near $V_{\text{int}} = -0.2$. The first cluster has $C \approx 1$ and $F_{|\Psi_+\rangle} \approx 1$, indicating that the maximally entangled Bell state $|\Psi_+\rangle$ is achieved with high fidelity for this system and parameters. Additionally, the high- and low-fidelity clusters do not significantly overlap in terms of V_{int}. These simulations show that homodyne measurements of the cavity transmission provide meaningful information regarding the fidelity of the final qubit state to the target.

Shown in Fig. 3 is a plot of the fidelity to target $F_{|\Psi_+\rangle}(\rho_{\text{cond,ps}})$ and concurrence $C(\rho_{\text{cond,ps}})$ of the postselected conditional final state, $\rho_{\text{cond,ps}} = 1/N_{\text{ps}}\sum_i \rho^i_{\text{cond,ps}}$, resulting from the ensemble of N_{ps} trajectories, $\rho^i_{\text{cond,ps}}$, postselected based on the integrated homodyne signal V_{int}. For Fig. 3, the criterion for postselection is $|V_{\text{int}}(t)| \leqslant t\sqrt{\Gamma_{\text{ci}}}$. This condition restricts the analysis to the ensemble of trajectories yielding an integrated homodyne signal V_{int} within the high-fidelity cluster in Fig. 2. The results presented in Ref. [32] were obtained in the strongly dispersive regime, but the specific value of g/Δ was neither relevant nor specified. Due to the computational cost of extending the simulation time out to the resulting $t_{\text{final}} \sim \Delta/g$, we opted to use a value of $g/\Delta = 0.1$.

Note that our simulated values of concurrence in Fig. 3 exhibit an initial oscillatory behavior that is not observed in Ref. [32]. We attribute these oscillations to the cavity-mediated interaction between the two qubits. First, we note that

$$\alpha(t) = \frac{2ip\sqrt{\kappa_{\text{in}}}}{\kappa} + c_\alpha e^{-t\kappa/2} \tag{14}$$

is a solution of Eq. (10) for constant c_α determined by the initial conditions. For the value of κ taken in Figs. 2 and 3, the second term of Eq. (14) decays quickly compared to the observed oscillation period. Thus, we assume a time-independent displacement α. After transforming Eq. (5) to the rotating reference frame defined by Eq. (6) with $\omega_d = \omega_c$, we apply the displacement operator $D[\alpha]$ with constant α. The dispersive Hamiltonian then takes the following form:

$$H_{\text{disp}} = \hbar\left(\sum_{j\in\{A,B\}} \chi_j \sigma_z^{(j)}\right)\left(\hat{a}^\dagger\hat{a} + |\alpha|^2 - \alpha^*\hat{a} - \alpha\hat{a}^\dagger + \frac{1}{2}\right) + \hbar J\left(\sigma_-^{(A)}\sigma_+^{(B)} + \sigma_+^{(A)}\sigma_-^{(B)}\right). \tag{15}$$

Our choice of the displaced reference frame as defined in Eq. (11) ensures that the cavity state is well approximated by the vacuum state, implying that the terms $\propto \hat{a}, \hat{a}^\dagger, \hat{a}^\dagger\hat{a}$ in Eq. (16) can be neglected. Employing this approximation and additionally requiring $\chi_A = \chi_B = \chi$, the time evolution generated by H_{disp} is given by

$$U(t) = \exp\left[-\frac{i}{\hbar}H_{\text{disp}}t\right] \tag{16}$$

$$= \exp\left[-i\chi\left(\frac{1}{2} + |\alpha|^2\right)\sigma_z^{(A)}t\right] \times \exp\left[-i\chi\left(\frac{1}{2} + |\alpha|^2\right)\sigma_z^{(B)}t\right] \times \exp\left[-iJ\left(\sigma_-^{(A)}\sigma_+^{(B)} + \sigma_+^{(A)}\sigma_-^{(B)}\right)t\right], \tag{17}$$

where the commutation relations

$$\left[\sigma_z^{(A)} + \sigma_z^{(B)}, \sigma_-^{(A)}\sigma_+^{(B)} + \sigma_+^{(A)}\sigma_-^{(B)}\right] = 0, \tag{18}$$

$$\left[\sigma_z^{(A)}, \sigma_z^{(B)}\right] = 0 \tag{19}$$

justify the breakdown of the exponential. The first two exponentials in Eq. (17) describe single qubit rotations of qubits A and B about the z-axis, respectively, and do not affect the entanglement dynamics between subsystems A and B. The third exponential, however, acts on both qubits; its matrix representation with respect to the basis $\{|\downarrow\rangle_A|\downarrow\rangle_B, |\downarrow\rangle_A|\uparrow\rangle_B, |\uparrow\rangle_A|\downarrow\rangle_B, |\uparrow\rangle_A|\uparrow\rangle_B\}$ is

$$U_{2q}(t) = \exp\left[-iJ(\sigma_-^{(A)}\sigma_+^{(B)} + \sigma_+^{(A)}\sigma_-^{(B)})t\right] \tag{20}$$

$$= \begin{bmatrix} 1 & 0 & 0 & 0 \\ 0 & \cos(Jt) & -i\sin(Jt) & 0 \\ 0 & -i\sin(Jt) & \cos(Jt) & 0 \\ 0 & 0 & 0 & 1 \end{bmatrix}. \tag{21}$$

This realizes a cavity-mediated entangling iSWAP gate for $Jt = (n + \frac{1}{2})\pi$ and $n \in \mathbb{N}_0$, while leaving the system unchanged for $Jt = n\pi$ [26,40,41]. The initial state $|\Psi_{\text{init}}\rangle$ evolves under the entangling interaction as

$$|\psi_{2q}(t)\rangle = U_{2q}(t)|{+x}\rangle_A|{+x}\rangle_B = \tfrac{1}{2}\{|\downarrow\rangle_A|\downarrow\rangle_B + [\cos(Jt) - i\sin(Jt)]|\downarrow\rangle_A|\uparrow\rangle_B + [\cos(Jt) - i\sin(Jt)]|\uparrow\rangle_A|\downarrow\rangle_B + |\uparrow\rangle_A|\uparrow\rangle_B\}. \tag{22}$$

The corresponding concurrence,

$$C(|\psi_{2q}(t)\rangle\langle\psi_{2q}(t)|) = |\sin(Jt)|, \tag{23}$$

inherits the time periodicity of $U_{2q}(t)$.

Figure 3 demonstrates the accuracy of our simulations: the long-term behavior of the concurrence is a close match to that produced by the dispersive model of Hutchison *et al.* [32] and the oscillations observed at short times are consistent with Eq. (23).

III. FLOPPING-MODE SPIN QUBIT MASTER EQUATION

We now consider two DQD flopping-mode spin qubits, again labeled A and B, coupled to a superconducting coplanar waveguide resonator. To derive the stochastic master equation for our MBE protocol, we begin with the (nondispersive) two-qubit Tavis-Cummings Hamiltonian [32,35,42], now with the full system Hamiltonian in the laboratory frame:

$$\tilde{H} = H_{\text{cavity}} + \sum_{j\in\{A,B\}}\left(\tilde{H}_{\text{DQD}}^{(j)} + \tilde{H}_{\text{inter}}^{(j)}\right), \tag{24}$$

$$H_{\text{cavity}} = \hbar\omega_c\hat{a}^\dagger\hat{a} + \hbar\sqrt{\kappa_{\text{in}}}[p(t)\hat{a}^\dagger e^{-i\omega_d t} + p^*(t)\hat{a}e^{i\omega_d t}], \tag{25}$$

$$\tilde{H}_{\text{DQD}}^{(j)} = \frac{\epsilon_j}{2}\tilde{\tau}_z^{(j)} + t_c^{(j)}\tilde{\tau}_x^{(j)} + \frac{B_z^{(j)}}{2}\sigma_z^{(j)} + \frac{b_x^{(j)}}{2}\tilde{\tau}_z^{(j)}\sigma_x^{(j)}, \tag{26}$$

$$\tilde{H}_{\text{inter}}^{(j)} = \hbar g_c^{(j)}(\hat{a}^\dagger + \hat{a})\tilde{\tau}_z^{(j)}, \tag{27}$$

where ϵ is the double-dot charge detuning, t_c is the interdot tunnel coupling, b_x is the energy associated with the transverse magnetic field difference between the dots, and B_z is the Zeeman energy due to the external magnetic field. The angular coupling frequency describing the interaction of the charge with the cavity electric field is g_c. $\tilde{\tau}_k$ and σ_k act on the charge (left or right dot occupation) and spin (up or down) degrees of freedom in Eq. (26).

After applying the sequence of transformations specified in the Appendix, we obtain the following effective Hamiltonian in the displaced and rotating frame:

$$\hat{H} = \hbar\Delta_c\hat{a}^\dagger\hat{a} + \sum_{j\in\{A,B\}}\left[\frac{\hbar}{2}\Delta_{\text{ch}}^{(j)}\hat{\tau}_z^{(j)} + \frac{\hbar}{2}\Delta_{\text{sp}}^{(j)}\hat{\sigma}_z^{(j)} + \hbar g_c^{(j)}\sin\left(\theta_1^{(j)} + \theta_2^{(j)}\right)\hat{\tau}_z^{(j)} \times ((\hat{a} - \alpha)\hat{\sigma}_+^{(j)} + (\hat{a}^\dagger - \alpha^*)\hat{\sigma}_-^{(j)}) + \hbar g_c^{(j)}\cos\left(\theta_1^{(j)} + \theta_2^{(j)}\right) \times ((\hat{a} - \alpha)\hat{\tau}_+^{(j)} + (\hat{a}^\dagger - \alpha^*)\hat{\tau}_-^{(j)})\right], \tag{28}$$

with the following definitions for each qubit:

$$\theta_{\substack{1\\2}} = \tan^{-1}\left(\sqrt{\left(\frac{2t_c \pm B_z}{b_x}\right)^2 + 1} - \left(\frac{2t_c \pm B_z}{b_x}\right)\right), \tag{29}$$

$$\omega_{\substack{1\\2}} = \frac{b_x}{2\hbar \sin\left(2\theta_{\substack{1\\2}}\right)}, \tag{30}$$

$$\omega_{\substack{\mathrm{ch}\\\mathrm{sp}}} = \omega_1 \pm \omega_2, \quad \Delta_{\substack{\mathrm{ch}\\\mathrm{sp}}} = \omega_{\substack{\mathrm{ch}\\\mathrm{sp}}} - \omega_d, \tag{31}$$

where α is the cavity coherent state population determined by Eq. (10). The Pauli operators $\{\hat{\tau}, \hat{\sigma}\}$ appearing in the DQD Hamiltonian [Eq. (28)] act on the eigenbasis $\{|0\rangle, |1\rangle, |2\rangle, |3\rangle\}$ with

$$\begin{aligned}
|0\rangle &= \cos\theta_1|-,\downarrow\rangle + \sin\theta_1|+,\uparrow\rangle,\\
|1\rangle &= \cos\theta_2|-,\uparrow\rangle + \sin\theta_2|+,\downarrow\rangle,\\
|2\rangle &= \cos\theta_2|+,\downarrow\rangle - \sin\theta_2|-,\uparrow\rangle,\\
|3\rangle &= \cos\theta_1|+,\uparrow\rangle - \sin\theta_1|-,\downarrow\rangle,
\end{aligned} \tag{32}$$

and the operators defined as

$$\begin{aligned}
\hat{\tau}_z\{|0\rangle, |1\rangle, |2\rangle, |3\rangle\} &= \{-|0\rangle, -|1\rangle, |2\rangle, |3\rangle\},\\
\hat{\tau}_-\{|0\rangle, |1\rangle, |2\rangle, |3\rangle\} &= \{0, 0, |0\rangle, |1\rangle\},\\
\hat{\sigma}_z\{|0\rangle, |1\rangle, |2\rangle, |3\rangle\} &= \{-|0\rangle, |1\rangle, -|2\rangle, |3\rangle\},\\
\hat{\sigma}_-\{|0\rangle, |1\rangle, |2\rangle, |3\rangle\} &= \{0, |0\rangle, 0, |2\rangle\}.
\end{aligned} \tag{33}$$

In the low field regime, i.e., $|B_z| < 2t_c$ (shaded green area in Fig. 4), the ground state to the first excited state transition energy is dominated by the Zeeman energy B_z, and the ground state to the second excited state transition energy is $\approx 2t_c$. Consequently, we can assign chargelike and spinlike properties to the DQD eigenstates, i.e., $\{|\widetilde{-,\downarrow}\rangle, |\widetilde{-,\uparrow}\rangle, |\widetilde{+,\downarrow}\rangle, |\widetilde{+,\uparrow}\rangle\}$ [40]. The five terms in Eq. (28) then correspond approximately to the cavity, charge, and spin energies, and to spin-photon and charge-photon coupling, respectively.

Now that we have described the coherent evolution of the two-qubit-cavity system, we can construct the master equation describing the time evolution of the full system density operator ρ in the presence of charge and spin dephasing,

$$\begin{aligned}
d\rho = \mathcal{L}_4\rho dt &= -\frac{i}{\hbar}[\hat{H}, \rho]dt\\
&+ \sum_{j\in\{A,B\}}\left(\frac{\gamma_{\substack{\mathrm{sp}\\}}^{(j)}}{2}\mathcal{D}\left[T\left(\sigma_z^{(j)}\right)\right]\rho + \frac{\gamma_{\substack{\mathrm{ch}\\}}^{(j)}}{2}\mathcal{D}\left[T\left(\tau_z^{(j)}\right)\right]\rho\right)dt\\
&+ \kappa(\mathcal{D}[\hat{a}]\rho)dt + \frac{\kappa}{2}[\alpha\hat{a}^\dagger - \alpha^*\hat{a}, \rho]dt,
\end{aligned} \tag{34}$$

where $\gamma_{\substack{\mathrm{sp}\\}}^{(j)}$, $\gamma_{\substack{\mathrm{ch}\\}}^{(j)}$, and κ are the spin dephasing, charge dephasing, and cavity decay rates, respectively, and $T(X)$ transforms an arbitrary operator X from the bonding-antibonding basis $\{|-\downarrow\rangle, |-\uparrow\rangle, |+\downarrow\rangle, |+\uparrow\rangle\}$ to the DQD eigenbasis $\{|0\rangle, |1\rangle, |2\rangle, |3\rangle\}$. The last term in Eq. (34) is a consequence of applying a displacement transformation to the cavity photon Lindblad term $\kappa\mathcal{D}[\hat{a}]\rho$ preceding it, and exactly cancels with the final term in Eq. (28). This cancellation is, in fact, the reason we added the term $-\frac{\kappa}{2}\alpha$ to our choice of $\dot{\alpha}$ in Eq. (10). Finally, we can obtain a stochastic master equation for homodyne readout using Eq. (11), replacing $\mathcal{L}$ with $\mathcal{L}_4$.

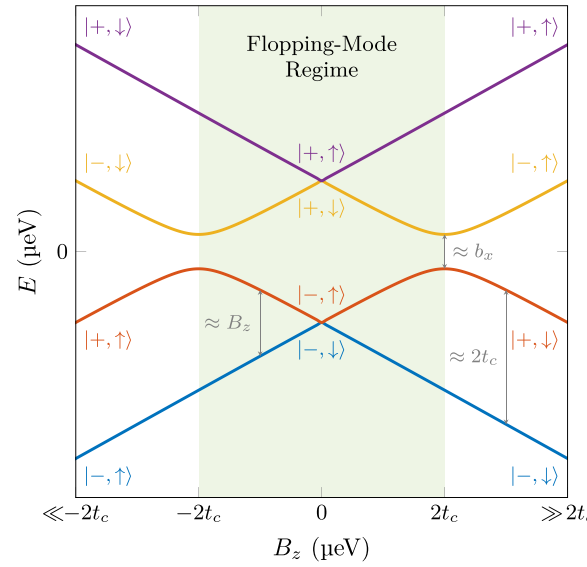

FIG. 4. Energy level structure of a flopping-mode spin qubit with a micromagnet as a function of external magnetic field ($\propto B_z$) for fixed interdot tunnel coupling t_c. The labels $|\mp,\downarrow\uparrow\rangle$ show the corresponding charge-spin eigenstates in each regime. For the MBE protocols described in this paper, the system is operated with $|B_z| < 2t_c$ (shaded in green). Here, the energy difference between the lowest two eigenstates is primarily spinlike, with a corresponding energy $\approx B_z$. The degree of spin-charge hybridization, and therefore the magnitude of the spin-photon coupling, increases as $|B_z| \to 2t_c$. In the regime where $B_z \gg 2t_c$, the transition between the two lowest eigenstates becomes primarily chargelike, with a corresponding transition energy $2t_c$.

To calculate the fidelity and concurrence of the final system state, we first trace out the cavity degree of freedom. Since

TABLE I. DQD device parameters taken from Ref. [40].

Quantity	Definition
$\left\|\psi_{\mathrm{initial}}^{\mathrm{qubit}}\right\rangle$	$\frac{1}{2}(\|0\rangle + \|1\rangle)^{\otimes 2}$
$\left\|\psi_{\mathrm{initial}}^{\mathrm{cavity}}\right\rangle$	$\|0\rangle$
$g_c^{(A)}/2\pi$	50 MHz
$g_c^{(B)}$	$-g_c^{(A)}$
$\kappa/2\pi$	1.5 MHz
t_c	13.2 μeV
B_z	24 μeV
b_x	2 μeV
ϕ	0 rad
η	1
$\alpha(\forall t)$	$0.1i$
$\gamma_{\mathrm{ch}}/2\pi$	2.5 MHz
$\gamma_{\mathrm{sp}}/2\pi$	0.005 MHz
$N_{\mathrm{trajs.}}$	1000
ω_d	ω_c
Δ_{sp}	$10g_c^{(A)}$
$\kappa_{\mathrm{in}}/\kappa_{\mathrm{out}}$	1/8

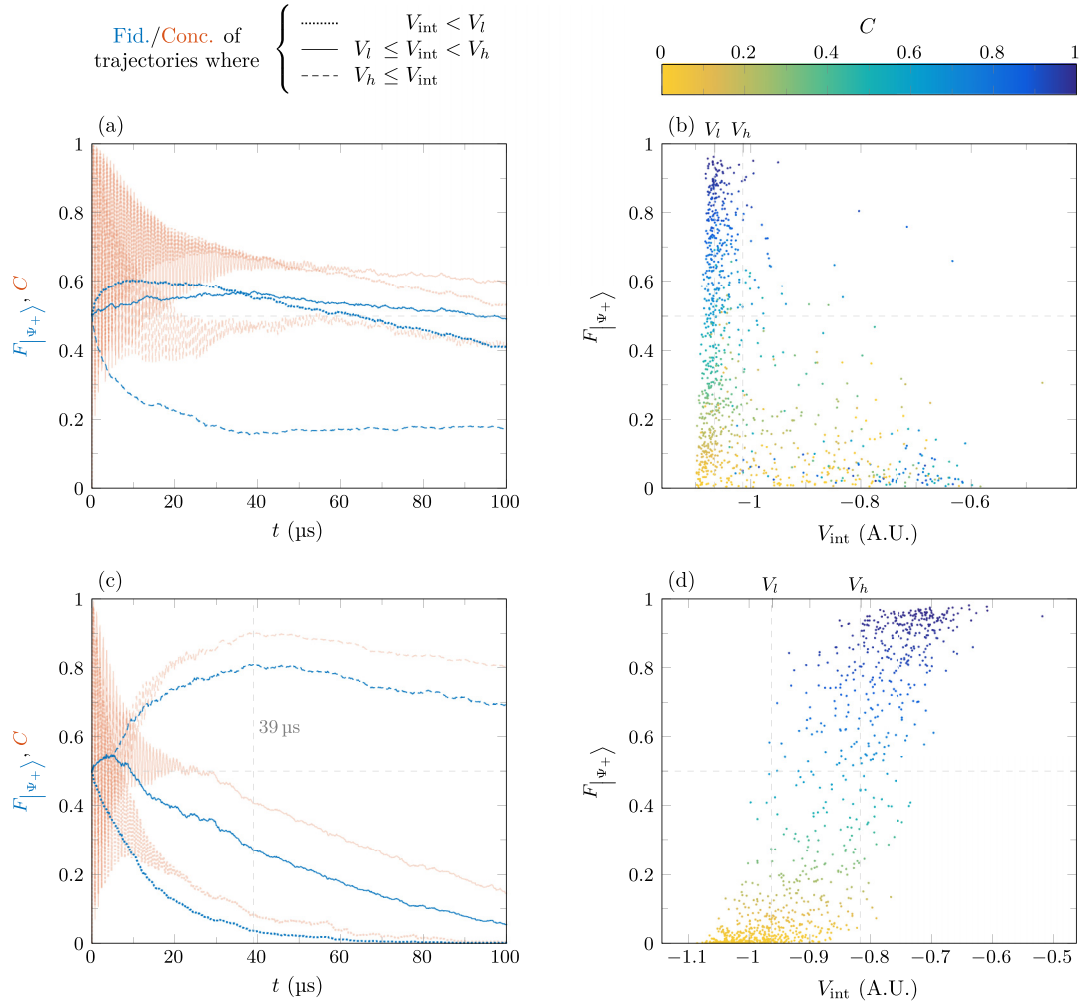

FIG. 5. (a) Plot of $F_{|\Psi_+\rangle}$ and C as a function of time for ensembles of trajectories with the lowest, middle, and highest third of corresponding $V_{\rm int}$ values, for the parameters listed in Table I. (b) Scatter plot of $F_{|\Psi_+\rangle}$ at $t = 100\,\mu$s as a function of $V_{\rm int}$ using the parameters given in Table I. The two vertical dashed lines indicate the upper (V_h) and lower (V_l) signal threshold values separating the data into the three groupings that are plotted with respect to time in (a). (c) Plot of $F_{|\Psi_+\rangle}$ and C as a function of time for the ensembles of trajectories with the lowest, middle, and highest third of corresponding $V_{\rm int}$ values, for a cavity decay rate $\kappa/2\pi = 15\,$MHz. All other parameters are the same as those given by Table I. (d) Scatter plot of $F_{|\Psi_+\rangle}$ at $t = 39\,\mu$s as a function of $V_{\rm int}$, for a cavity decay rate $\kappa/2\pi = 15\,$MHz. All other parameters are the same as those given in Table I.

the resulting system consists of two four-level systems, we must also trace out the chargelike degrees of freedom for both DQDs to produce $\rho_{\rm red} = {\rm Tr}_{\rm ch}[{\rm Tr}_{\rm cav}[\rho_{\rm cond}]]$. While tracing out the cavity degree of freedom is straightforward, the trace over the chargelike degree of freedom requires some clarification: Denoting the spinlike qubit states by $|\widetilde{\zeta}\rangle_j$ with $j \in \{A, B\}$ and $\zeta \in \{\downarrow, \uparrow\}$, the matrix elements of $\rho_{\rm red.}$ are defined by

$$
\begin{aligned}
&{}_A\langle\widetilde{\zeta}|_B\langle\widetilde{\xi}|\rho_{\rm red}|\widetilde{\zeta'}\rangle_A|\widetilde{\xi'}\rangle_B \\
&\quad = \sum_{k,l\in\{-,+\}} {}_A\langle\widetilde{k,\zeta}|_B\langle\widetilde{l,\xi}|{\rm Tr}_{\rm cav}[\rho_{\rm cond}]|\widetilde{k,\zeta'}\rangle_A|\widetilde{l,\xi'}\rangle_B \quad (35)
\end{aligned}
$$

for $\zeta, \xi, \zeta', \xi' \in \{\downarrow, \uparrow\}$. The spin-charge hybridized states $|\widetilde{k,\zeta}\rangle_j$ can be identified with the DQD Hamiltonian eigenstates $\{|0\rangle, |1\rangle, |2\rangle, |3\rangle\}$ as explained above. Since $\rho_{\rm red}$ is a 4×4 density matrix corresponding to the spinlike states of the two DQDs, we can calculate $F_{|\Psi_+\rangle}$ and C as we did for the two-level qubit model.

IV. RESULTS

We can now simulate entanglement generation for flopping-mode spin-qubit cQED devices accounting for both the spin and charge degrees of freedom. The simulations are performed by numerically solving Eq. (11) with $\mathcal{L}$ substituted by $\mathcal{L}_4$ defined in Eq. (34), which in turn requires the Hamiltonian Eq. (28). The system parameters used for the simulation shown in Table I are taken from a device designed to perform dispersive *coherent* two-qubit operations [40], i.e., a cavity iSWAP. The result of simulating 1000 trajectories of the stochastic master equation is shown in Figs. 5(a) and 5(b). We can visualize the protocol's effect over time by dividing the set of trajectories into three groups based on their integrated signal at each time: one containing the third of trajectories with the lowest $V_{\rm int}$ ($V_{\rm int} < V_l$), one containing the third with the highest $V_{\rm int}$ ($V_{\rm int} \geqslant V_h$) and one containing the remaining trajectories ($V_l \leqslant V_{\rm int} < V_h$). These groupings

define the lower, V_l, and upper, V_h, signal threshold values. We can then plot the fidelity to target and concurrence for each of these ensembles over the duration of the measurement. Such a plot is shown in Fig. 5(a). Although the measurement achieves a fidelity to $F_{|\Psi_+\rangle}$ greater than 50% for the lowest and middle thirds of V_{int} values, the inability to postselect for higher-fidelity states causes the achievable average fidelity to reach a maximum of 61% for these device parameters.

Figure 5(b) shows a scatter plot $F_{|\Psi_+\rangle}$ as a function of V_{int} with a measurement time of 100 μs. The trajectories have a wide range of fidelities between 0% and 95%. A correlation between V_{int} and $F_{|\Psi_+\rangle}$ is evident; however, the slope of this correlation is much too high to reliably postselect for high-fidelity states, given the nonzero spread in V_{int} for trajectories of equal fidelity. In principle, we could simply increase the measurement time further, allowing the trajectories to form high- and low-fidelity clusters with a resolvable V_{int} separation. However, the spin dephasing time $2\pi/\gamma_{\text{sp}} = 200\,\mu\text{s}$ establishes an upper bound for usable measurement times, since states measured over a time $t \sim 200\,\mu\text{s}$ will be subject to significant spin dephasing before the measurement is complete.

One approach to improve MBE performance is to increase the cavity outcoupling rate κ, which will increase the magnitude of the stochastic term in Eq. (11) and therefore increase the relative effect of the measurement on the final qubit state. In Figs. 5(c) and 5(d), we examine the result of a 10× increase in κ. The increase in κ results in a significant enhancement in the overall MBE protocol fidelity: the fidelity of the ensemble of trajectories with the highest third of integrated homodyne outputs V_{int} is $F_{|\Psi_+\rangle} = 81\%$, as shown in Fig. 5(c). Figure 5(d) provides additional information on the relationship between $F_{|\Psi_+\rangle}$, V_{int}, and C) at the final measurement time of 39 μs. In the upper right portion of Fig. 5(d), we observe the cluster of trajectories that have been projected onto the target $|\Psi_+\rangle$, with a peak $F_{|\Psi_+\rangle} = 98\%$ and $F_{|\Psi_+\rangle} = 81\%$ for the postselected ensemble of trajectories corresponding to the third of the homodyne measurement results with the highest V_{int}.

Figure 6 shows how $F_{|\Psi_+\rangle}$ and C respond to changes in the postselection yield. For the data in Fig. 5(d), we select trajectories with V_{int} *greater than* a threshold. We use the postselection yield Y, the fraction of trajectories satisfying the postselection criteria, in place of the associated maximum V_{int}. The solid lines in Fig. 6 present equivalent information corresponding to a device with an increased outcoupling rate $\kappa/2\pi = 15\,\text{MHz}$, at time $t = 39\,\mu\text{s}$. As the postselection yield is reduced, the fidelity $F_{|\Psi_+\rangle}$ of the postselected ensemble rises, eventually reaching a maximum value of ∼95%. The concurrence similarly increases to a maximum value of ∼99% for low yields. A more realistic postselection yield of 33% can, as mentioned previously, achieve a reasonable fidelity of ∼81%; this yield is indicated by the dashed vertical line in Fig. 6.

Overall, if we are willing to discard a sufficient fraction of measurement runs, increasing the cavity outcoupling rate to $\kappa/2\pi = 15\,\text{MHz}$ results in significant improvements to the Bell-state fidelity and concurrence of the postselected two-qubit state. Based on these observations, we predict that a DQD-based cQED device with $\kappa/2\pi = 15\,\text{MHz}$ and other parameters specified by Table I, would be capable of a demonstration of MBE.

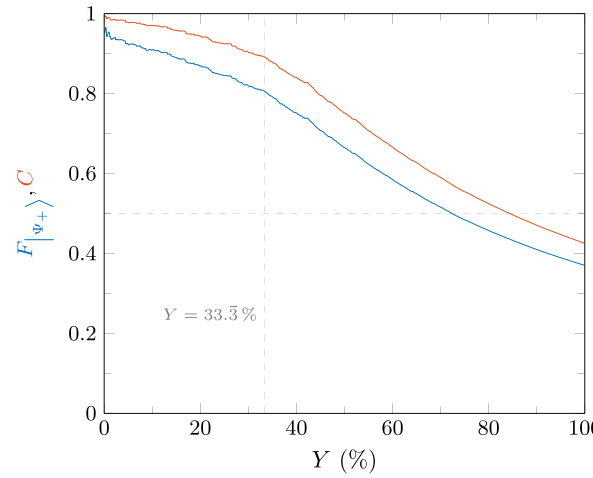

FIG. 6. Plot of $F_{|\Psi_+\rangle}$ (blue) and C (orange), when postselecting the $Y\%$ of trajectories with the highest values of V_{int}. These simulations correspond to $\kappa/2\pi = 15\,\text{MHz}$ and a measurement time of 39 μs, i.e., the data in Fig. 5(d).

V. CONCLUSIONS

We have developed a theoretical model to simulate the evolution of two silicon flopping mode spin qubits coupled to a microwave resonator and subjected to a continuous homodyne-based parity measurement. Results from these simulations suggest that current Si/SiGe DQD cavity devices, designed to utilize photon-mediated spin-spin coupling, would only be able to achieve a fidelity to the target Bell state $|\Psi_+\rangle$ of ∼61% when subjected to realistic levels of charge and spin dephasing. A device better suited to such an experiment would likely need to incorporate an output cavity coupling rate ∼10× higher than current devices. Simulations indicate that with such a cavity, the device would be able to achieve a fidelity to the target Bell state $|\Psi_+\rangle$ of 81% at a predicted 33% postselection success probability, based on a homodyne measurement of the cavity output.

ACKNOWLEDGMENT

Supported by Army Research Office Grants No. W911NF-15-1-0149 and No. W911NF-23-1-0104.

APPENDIX: DETAILED DERIVATION OF THE EFFECTIVE HAMILTONIAN

As the qubits have no direct interactions with each other, for the moment we will omit the sum over the two qubits and examine the Hamiltonian of a single qubit coupled to the cavity. Since we do not make a dispersive approximation, we will not perform any changes of basis that hybridize qubit and cavity states; obtaining the two-qubit Hamiltonian from the single-qubit version is therefore straightforward.

In the case of zero charge detuning ($\epsilon = 0$), the eigenbasis of the charge-qubit Hamiltonian $H_{\text{charge}} = t_c\tilde{\tau}_x$ is simply the bonding-antibonding basis, $|\mp\rangle = \frac{1}{\sqrt{2}}(|R\rangle \mp |L\rangle)$.

Writing our charge-state Pauli operators as τ after transforming to this basis, we find that $\tilde{\tau}_z \to \tau_x$ and $\tilde{\tau}_x \to \tau_z$. Therefore, our Hamiltonian from Eq. (24) becomes:

$$H = H_{\text{cavity}} + H_{\text{DQD}} + H_{\text{inter}}, \tag{A1}$$

$$H_{\text{DQD}} = t_c\tau_z + \frac{B_z}{2}\sigma_z + \frac{b_x}{2}\tau_x\sigma_x, \tag{A2}$$

$$H_{\text{inter}} = \hbar g_c(\hat{a}^\dagger + \hat{a})\tau_x, \tag{A3}$$

with H_{cavity} as defined in Eq. (25).

As shown in Eq. (A2), the electron spin states couple to the electron charge states via a micromagnet-induced magnetic field gradient, which produces the spin-dependent interdot energy difference b_x. The DQD charge states in turn couple to the cavity field via a typical dipole field term, shown in Eq. (A3).

We now perform another change of basis, this time to diagonalize H_{DQD} as given in Eq. (A2). After diagonalizing, we are able to define ω_1, ω_2 such that the eigenfrequencies of H_{DQD} are $\{-\omega_1, -\omega_2, \omega_2, \omega_1\}$.

In the DQD eigenbasis given in Eq. (32), our Hamiltonian becomes

$$\hat{H} = H_{\text{cavity}} + \hat{H}_{\text{qubit}} + \hat{H}_{\text{inter}}, \tag{A4}$$

$$\hat{H}_{\text{DQD}} = \hbar\omega_1(\hat{\Pi}_3 - \hat{\Pi}_0) + \hbar\omega_2(\hat{\Pi}_2 - \hat{\Pi}_1), \tag{A5}$$

$$\hat{H}_{\text{inter}} = \hbar g_c(\hat{a}^\dagger + \hat{a})\tau_x, \tag{A6}$$

where $\hat{\Pi}_k = |k\rangle\langle k|$ is the projector onto DQD eigenstate $|k\rangle$ ($k \in \{0, 1, 2, 3\}$) given in Eq. (32), and H_{cavity} is as defined in Eq. (25). Transforming τ_x to the DQD eigenbasis, we find

$$\tau_x \to \cos(\theta_1 + \theta_2)\hat{\tau}_x + \sin(\theta_1 + \theta_2)\hat{\tau}_z\hat{\sigma}_x, \tag{A7}$$

where the Pauli operators $\hat{\tau}_i$ and $\hat{\sigma}_i$ are defined in Eq. (33).

If we additionally transform to a rotating frame via the transformation $V = e^{-i\hat{H}_{\text{DQD}}t/\hbar}$, the DQD Hamiltonian vanishes, while inside the interaction Hamiltonian, τ_x becomes

$$\begin{aligned}&\cos(\theta_1 + \theta_2)(e^{-i(\omega_1+\omega_2)t}\hat{\tau}_- + e^{i(\omega_1+\omega_2)t}\hat{\tau}_+)\\ &+ \sin(\theta_1 + \theta_2)\hat{\tau}_z(e^{-i(\omega_1-\omega_2)t}\hat{\sigma}_- + e^{i(\omega_1-\omega_2)t}\hat{\sigma}_+).\end{aligned} \tag{A8}$$

Due to the association of the quantities $\omega_1 + \omega_2$ and $\omega_1 - \omega_2$ with charge and spin transitions, respectively, we define $\omega_{\text{ch}} = \omega_1 + \omega_2$ and $\omega_{\text{sp}} = \omega_1 - \omega_2$. These are the chargelike and spinlike frequencies of the hybridized qubit.

We now turn our attention to the cavity Hamiltonian given in Eq. (25). To eliminate the terms in this equation proportional to $p(t)$, we first transform to a rotating reference frame. The transformation is specified by the operator $W = e^{-i\omega_d\hat{a}^\dagger\hat{a}t}$. Applying W to Eq. (25), we obtain

$$H'_{\text{cavity}} = \hbar\overbrace{(\omega_c - \omega_d)}^{\equiv\Delta_c}\hat{a}^\dagger\hat{a} + \hbar\sqrt{\kappa_{\text{in}}}(p(t)\hat{a}^\dagger + p^*(t)\hat{a}). \tag{A9}$$

We then apply a displacement transformation $D[\alpha] \equiv e^{\alpha\hat{a}^\dagger - \alpha^*\hat{a}}$, obtaining

$$\begin{aligned}\hat{H}_{\text{cavity}} &= \hbar\Delta_c(\hat{a}^\dagger\hat{a} + |\alpha|^2)\\ &\quad - \hbar\sqrt{\kappa_{\text{in}}}(p\alpha^* + p^*\alpha) + \frac{i\hbar}{2}(\alpha\dot{\alpha}^* - \alpha^*\dot{\alpha})\\ &\quad + \hbar(\sqrt{\kappa_{\text{in}}}p - \Delta_c\alpha + i\dot{\alpha})\hat{a}^\dagger\\ &\quad + \hbar(\sqrt{\kappa_{\text{in}}}p^* - \Delta_c\alpha^* - i\dot{\alpha}^*)\hat{a}.\end{aligned} \tag{A10}$$

An intuitive choice for α would be $\dot{\alpha} \equiv -i\Delta_c\alpha + i\sqrt{\kappa_{\text{in}}}p(t)$, which would nullify the final two terms in Eq. (A10). This would be appropriate if simplifying the Hamiltonian were our only concern. With the benefit of hindsight, we instead select $\dot{\alpha} \equiv -i\Delta_c\alpha + i\sqrt{\kappa_{\text{in}}}p(t) - \frac{\kappa}{2}\alpha$, for some as yet undefined κ. With this choice, Eq. (A10) reduces to

$$\hat{H}_{\text{cavity}} = \hbar\Delta_c\hat{a}^\dagger\hat{a} - \frac{\hbar}{2}\sqrt{\kappa_{\text{in}}}(p\alpha^* + p^*\alpha) - \frac{i\hbar}{2}\kappa(\alpha\hat{a}^\dagger - \alpha^*\hat{a}). \tag{A11}$$

The second term in Eq. (A11) is a state-independent constant and can therefore be discarded.

We now apply the cavity rotation and displacement transformations to the interaction term in Eq. (A6). From this, we obtain

$$\begin{aligned}\hat{H} &= \hbar\Delta_c\hat{a}^\dagger\hat{a} + \hbar g_c\big(e^{i\omega_d t}(\hat{a}^\dagger - \alpha^*) + e^{-i\omega_d}(\hat{a} - \alpha)\big)\tau_x\\ &\quad - \frac{i\hbar}{2}\kappa(\alpha\hat{a}^\dagger - \alpha^*\hat{a}),\end{aligned} \tag{A12}$$

with τ_x taking the form given in Eq. (A8).

Finally, we can make a rotating-wave approximation, assuming that $\{\omega_{\text{ch}} - \omega_d, \omega_{\text{sp}} - \omega_d\} \ll \{\omega_{\text{ch}} + \omega_d, \omega_{\text{sp}} + \omega_d\}$. This allows us to eliminate rapidly oscillating subterms from the second term of Eq. (A12), to obtain

$$\hat{H} = \hbar\Delta_c\hat{a}^\dagger\hat{a} + \hbar g_c\{(\hat{a}^\dagger - \alpha^*)[e^{-i\Delta_{\text{ch}}t}\cos(\theta_1 + \theta_2)\hat{\tau}_- + e^{-i\Delta_{\text{sp}}t}\sin(\theta_1 + \theta_2)\hat{\tau}_z\hat{\sigma}_-] + \text{H.c.}\} - \frac{i\hbar}{2}\kappa(\alpha\hat{a}^\dagger - \alpha^*\hat{a}), \tag{A13}$$

where $\Delta_{\text{ch}} = \omega_{\text{ch}} - \omega_d$ and $\Delta_{\text{sp}} = \omega_{\text{sp}} - \omega_d$.

If we apply two additional rotating frame transformations, defined by $V_{\text{ch}} = e^{\frac{1}{2}i\Delta_{\text{ch}}\hat{\tau}_z t}$ and $V_{\text{sp}} = e^{\frac{1}{2}i\Delta_{\text{sp}}\hat{\sigma}_z t}$, we obtain Eq. (28), a Hamiltonian that contains no explicit time dependence once its final term cancels with the corresponding term in Eq. (34).

[1] G. Burkard, T. D. Ladd, A. Pan, J. M. Nichol, and J. R. Petta, Rev. Mod. Phys. **95**, 025003 (2023).

[2] J. R. Petta, A. C. Johnson, J. M. Taylor, E. A. Laird, A. Yacoby, M. D. Lukin, C. M. Marcus, M. P. Hanson, and A. C. Gossard, Science **309**, 2180 (2005).

[3] D. M. Zajac, A. J. Sigillito, M. Russ, F. Borjans, J. M. Taylor, G. Burkard, and J. R. Petta, Science **359**, 439 (2018).

[4] T. F. Watson, S. G. J. Philips, E. Kawakami, D. R. Ward, P. Scarlino, M. Veldhorst, D. E. Savage, M. G. Lagally, M. Friesen, S. N. Coppersmith, M. A. Eriksson,

and L. M. K. Vandersypen, Nature (London) **555**, 633 (2018).
[5] A. Noiri, K. Takeda, T. Nakajima, T. Kobayashi, A. Sammak, G. Scappucci, and S. Tarucha, Nature (London) **601**, 338 (2022).
[6] X. Xue, M. Russ, N. Samkharadze, B. Undseth, A. Sammak, G. Scappucci, and L. M. K. Vandersypen, Nature (London) **601**, 343 (2022).
[7] A. R. Mills, C. R. Guinn, M. J. Gullans, A. J. Sigillito, M. M. Feldman, E. Nielsen, and J. R. Petta, Sci. Adv. **8**, eabn5130 (2022).
[8] C. H. Bennett, G. Brassard, C. Crépeau, R. Jozsa, A. Peres, and W. K. Wootters, Phys. Rev. Lett. **70**, 1895 (1993).
[9] A. K. Ekert, Phys. Rev. Lett. **67**, 661 (1991).
[10] C. H. Bennett, G. Brassard, and N. D. Mermin, Phys. Rev. Lett. **68**, 557 (1992).
[11] M. Caleffi, M. Amoretti, D. Ferrari, D. Cuomo, J. Illiano, A. Manzalini, and A. S. Cacciapuoti, arXiv:2212.10609.
[12] A. Blais, R.-S. Huang, A. Wallraff, S. M. Girvin, and R. J. Schoelkopf, Phys. Rev. A **69**, 062320 (2004).
[13] A. Wallraff, D. I. Schuster, A. Blais, L. Frunzio, R.-S. Huang, J. Majer, S. Kumar, S. M. Girvin, and R. J. Schoelkopf, Nature (London) **431**, 162 (2004).
[14] J. Majer, J. M. Chow, J. M. Gambetta, J. Koch, B. R. Johnson, J. A. Schreier, L. Frunzio, D. I. Schuster, A. A. Houck, A. Wallraff, A. Blais, M. H. Devoret, S. M. Girvin, and R. J. Schoelkopf, Nature (London) **449**, 443 (2007).
[15] M. A. Sillanpää, J. I. Park, and R. W. Simmonds, Nature (London) **449**, 438 (2007).
[16] A. Cottet and T. Kontos, Phys. Rev. Lett. **105**, 160502 (2010).
[17] T. Frey, P. J. Leek, M. Beck, A. Blais, T. Ihn, K. Ensslin, and A. Wallraff, Phys. Rev. Lett. **108**, 046807 (2012).
[18] K. D. Petersson, L. W. McFaul, M. D. Schroer, M. Jung, J. M. Taylor, A. A. Houck, and J. R. Petta, Nature (London) **490**, 380 (2012).
[19] X. Mi, M. Benito, S. Putz, D. M. Zajac, J. M. Taylor, G. Burkard, and J. R. Petta, Nature (London) **555**, 599 (2018).
[20] N. Samkharadze, G. Zheng, N. Kalhor, D. Brousse, A. Sammak, U. C. Mendes, A. Blais, G. Scappucci, and L. M. K. Vandersypen, Science **359**, 1123 (2018).
[21] A. J. Landig, J. V. Koski, P. Scarlino, U. C. Mendes, A. Blais, C. Reichl, W. Wegscheider, A. Wallraff, K. Ensslin, and T. Ihn, Nature (London) **560**, 179 (2018).
[22] F. Borjans, X. G. Croot, X. Mi, M. J. Gullans, and J. R. Petta, Nature (London) **577**, 195 (2020).
[23] P. Harvey-Collard, J. Dijkema, G. Zheng, A. Sammak, G. Scappucci, and L. M. K. Vandersypen, Phys. Rev. X **12**, 021026 (2022).
[24] J. Dijkema, X. Xue, P. Harvey-Collard, M. Rimbach-Russ, S. L. de Snoo, G. Zheng, A. Sammak, G. Scappucci, and L. M. K. Vandersypen, arXiv:2310.16805.
[25] P. Krantz, M. Kjaergaard, F. Yan, T. P. Orlando, S. Gustavsson, and W. D. Oliver, Appl. Phys. Rev. **6**, 021318 (2019).
[26] S. M. Young, N. T. Jacobson, and J. R. Petta, Phys. Rev. Appl. **18**, 064082 (2022).
[27] C. Cabrillo, J. I. Cirac, P. García-Fernández, and P. Zoller, Phys. Rev. A **59**, 1025 (1999).
[28] B. P. Lanyon, P. Jurcevic, M. Zwerger, C. Hempel, E. A. Martinez, W. Dür, H. J. Briegel, R. Blatt, and C. F. Roos, Phys. Rev. Lett. **111**, 210501 (2013).
[29] D. Ristè, J. G. van Leeuwen, H.-S. Ku, K. W. Lehnert, and L. DiCarlo, Phys. Rev. Lett. **109**, 050507 (2012).
[30] W. Pfaff, T. H. Taminiau, L. Robledo, H. Bernien, M. Markham, D. J. Twitchen, and R. Hanson, Nat. Phys. **9**, 29 (2013).
[31] D. Ristè, M. Dukalski, C. A. Watson, G. de Lange, M. J. Tiggelman, Y. M. Blanter, K. W. Lehnert, R. N. Schouten, and L. DiCarlo, Nature (London) **502**, 350 (2013).
[32] C. L. Hutchison, J. M. Gambetta, A. Blais, and F. K. Wilhelm, Can. J. Phys. **87**, 225 (2009).
[33] K. Lalumière, J. M. Gambetta, and A. Blais, Phys. Rev. A **81**, 040301(R) (2010).
[34] X.-Y. Zhu, T. Tu, G.-C. Guo, and C.-F. Li, Phys. Rev. A **107**, 033708 (2023).
[35] M. Benito, X. Mi, J. M. Taylor, J. R. Petta, and G. Burkard, Phys. Rev. B **96**, 235434 (2017).
[36] A. Blais, J. Gambetta, A. Wallraff, D. I. Schuster, S. M. Girvin, M. H. Devoret, and R. J. Schoelkopf, Phys. Rev. A **75**, 032329 (2007).
[37] H. M. Wiseman and G. J. Milburn, *Quantum Measurement and Control* (Cambridge University Press, Cambridge, UK, 2009).
[38] P. E. Kloeden and E. Platen, *Numerical Solution of Stochastic Differential Equations*, 3rd ed. (Springer, Berlin, 1992).
[39] W. K. Wootters, Phys. Rev. Lett. **80**, 2245 (1998).
[40] M. Benito, X. Croot, C. Adelsberger, S. Putz, X. Mi, J. R. Petta, and G. Burkard, Phys. Rev. B **100**, 125430 (2019).
[41] J. Mielke and G. Burkard, Phys. Rev. B **107**, 155302 (2023).
[42] M. Tavis and F. W. Cummings, Phys. Rev. **170**, 379 (1968).